

# Representing the boundary of stellarator plasmas

S.A. Henneberg<sup>1,†</sup>, P. Helander<sup>1</sup> and M. Drevlak<sup>1</sup>

<sup>1</sup>Max-Planck-Institut für Plasmaphysik, Wendelsteinstr. 1, 17489 Greifswald, Germany

(Received 25 May 2021; revised 18 August 2021; accepted 23 August 2021)

In stellarator optimization studies, the boundary of the plasma is usually described by Fourier series that are not unique: several sets of Fourier coefficients describe approximately the same boundary shape. A simple method for eliminating this arbitrariness is proposed and shown to work well in practice.

## 1. Introduction

In optimized stellarators, the magnetic field lines usually trace out simply nested flux surfaces. Large magnetic islands or regions with chaotic field lines are avoided, at least in the plasma core, in the interest of good confinement. Kruskal and Kulsrud have shown that magnetostatic equilibria with this property (insofar as they exist) are uniquely determined by the shape of the toroidal boundary and by the plasma current and pressure profiles (Kruskal & Kulsrud 1958; Helander 2014). The rotational transform profile can be used in place of the current profile to uniquely determine the equilibrium.

This fundamental result provides the theoretical basis for fixed-boundary magnetohydrodynamic (MHD) equilibrium calculations, which are commonly used in stellarator optimization studies. The shape of the plasma boundary is prescribed, usually as a Fourier series in poloidal and toroidal angles (Hirshman & Whitson 1983; Nührenberg & Zille 1988),

$$\left. \begin{aligned} R(\theta, \varphi) &= \sum_{m=0}^M \sum_{n=-N}^N R_{m,n} \cos(m\theta - n\varphi), \\ Z(\theta, \varphi) &= \sum_{m=0}^M \sum_{n=-N}^N Z_{m,n} \sin(m\theta - n\varphi), \end{aligned} \right\} \quad (1.1)$$

and provides input to a fixed-boundary MHD equilibrium code. Here  $(R, \varphi, Z)$  denote cylindrical coordinates and  $\theta$  is a ‘poloidal’ angle parameter, whose choice is the topic of this paper. For simplicity, we restrict our attention to fields with stellarator symmetry,

$$\left. \begin{aligned} R(\theta, \varphi) &= R(-\theta, -\varphi), \\ Z(\theta, \varphi) &= -Z(-\theta, -\varphi). \end{aligned} \right\} \quad (1.2)$$

† Email address for correspondence: [sophia.henneberg@ipp.mpg.de](mailto:sophia.henneberg@ipp.mpg.de)

Relinquishing this symmetry is not difficult, but the number of coefficients then needs to be doubled because one has to include the coefficients of the opposite parity.

In stellarator optimization, the Fourier coefficients  $R_{m,n}$  and  $Z_{m,n}$  are varied until an optimal magnetic equilibrium has been found, where the optimum is defined by the minimum of some optimization target function. The optimization thus amounts to a search in a space of  $2(M+1)(2N+1)$  dimensions.<sup>1</sup> However, as has sometimes been remarked (Lee *et al.* 1988; Hirshman & Breslau 1998), this representation is not unique but contains ‘tangential degrees of freedom’ in the limit  $M \rightarrow \infty, N \rightarrow \infty$ . If a large but finite number of terms are included in the Fourier series, several very different choices of the coefficients  $\{R_{mn}, Z_{mn}\}$  correspond to approximately the same surface shape. Unless this problem is addressed, the search is therefore performed in a space of unnecessarily large dimensionality. Hirshman and co-workers devised a method called ‘spectral condensation’ to deal with this problem, which is used internally in the VMEC and SPEC equilibrium codes to minimize the number of coefficients in the Fourier representation of all magnetic surfaces, including interior ones (Hirshman & Whitson 1983; Hirshman & Van Rij 1986; Hudson *et al.* 2012). However, spectral condensation is rarely used for the plasma boundary in optimization studies. The present article suggests another method for dealing with the problem of non-uniqueness of the boundary representation. This method is simpler but mathematically less sophisticated than spectral condensation. Unlike the latter, it does not correspond to a representation that is optimally economical, but it is simpler to implement numerically, requires less computation and appears to work quite well in practice.

The remainder of the present paper first describes the non-uniqueness of the representation (1.1) and how it can be eliminated, followed by examples showing how this technique simplifies the problem of optimization by eliminating a plethora of spurious and approximate minima of the target function in configuration space.

## 2. Non-uniqueness of the usual representation

In the representation (1.1), the variable  $\varphi$  denotes the toroidal geometric angle, but the choice of poloidal angle  $\theta$  is arbitrary. Indeed, if we define

$$\left. \begin{aligned} \tilde{R}(\theta, \varphi) &= R(\theta + \epsilon(\theta, \varphi), \varphi), \\ \tilde{Z}(\theta, \varphi) &= Z(\theta + \epsilon(\theta, \varphi), \varphi), \end{aligned} \right\} \quad (2.1)$$

where  $\epsilon$  is any continuous, doubly  $2\pi$ -periodic function,<sup>2</sup> then the surfaces

$$S = \{(x, y, z) = (R(\theta, \varphi) \cos \varphi, R(\theta, \varphi) \sin \varphi, Z(\theta, \varphi)) : 0 \leq \theta < 2\pi, 0 \leq \varphi < 2\pi\} \quad (2.2)$$

and

$$\tilde{S} = \{(x, y, z) = (\tilde{R}(\theta, \varphi) \cos \varphi, \tilde{R}(\theta, \varphi) \sin \varphi, \tilde{Z}(\theta, \varphi)) : 0 \leq \theta < 2\pi, 0 \leq \varphi < 2\pi\} \quad (2.3)$$

coincide. Moreover, if  $|\partial\epsilon(\theta, \varphi)/\partial\theta| < 1$  for all  $\theta$  and  $\varphi$ , then both surface parametrizations are bijective if one of them has this property.

The fact that the addition of the function  $\epsilon(\theta, \varphi)$  to the poloidal angle  $\theta$  does not change  $S$  indicates great freedom in the parametrization of the surface. If  $M = N = \infty$  in the sum (1.1), then infinitely many choices of coefficients  $\{R_{mn}, Z_{mn}\}$  generate the same surface.

<sup>1</sup>Usually, the number is in fact slightly smaller, because negative values of  $n$  and  $n = 0$  are not included in the terms with  $m = 0$ .

<sup>2</sup>For simplicity, we take  $\epsilon$  to satisfy  $\epsilon(-\theta, -\varphi) = -\epsilon(\theta, \varphi)$  to preserve stellarator symmetry in the series (1.1).

Note that very different sets of coefficients can describe the same surface. However, if  $M$  and  $N$  are finite in (1.1), so that the Fourier series of the functions  $R(\theta, \varphi)$  and  $Z(\theta, \varphi)$  terminate after a finite number of terms, then the corresponding series for  $\tilde{R}(\theta, \varphi)$  and  $\tilde{Z}(\theta, \varphi)$  will, in general, not terminate.

This observation has implications for the nature of the representation (1.1) when  $M$  and  $N$  are fixed, finite numbers:

- (i) If  $M$  and  $N$  are not too large, so that only a few terms are kept in the series (1.1), then the surface it represents will usually correspond to a unique set of coefficients  $\{R_{m,n}, Z_{m,n}\}$  or a small number of such sets. Of course, with only a few harmonics, not every surface can be represented by the series (1.1).
- (ii) However, if many terms are included in the sum,  $M \sim N \gg 1$ , so that almost any stellarator-symmetric surface can be described by the series (1.1), then many widely different choices of coefficients  $\{R_{m,n}, Z_{m,n}\}$  can correspond to almost the same surface. The more harmonics allowed in the sum will result in the representation becoming less unique.

These observations are confirmed by practical experience. At the beginning of a stellarator optimization run, it is usually futile to include many Fourier harmonics in the representation of the plasma boundary; the optimization then ‘gets stuck’ and does not proceed far from the initial state. Instead, it often proves useful to begin with only a few harmonics and gradually add more terms as the optimization proceeds, to allow for greater freedom in the shape of the plasma.

### 3. Spectral condensation

Spectral condensation exploits the non-uniqueness of the poloidal angle by minimizing the ‘spectral width’, which measures the spectral extent of  $R_{mn}$  and  $Z_{mn}$ , under the constraint of not changing the geometry of the surface  $S$ . The spectral width is defined by Hirshman & Meier (1985) and Hirshman & Breslau (1998) as

$$M \equiv \frac{\sum_{m,n} m^{(p+q)} (R_{m,n}^2 + Z_{m,n}^2)}{\sum_{m,n} m^p (R_{m,n}^2 + Z_{m,n}^2)}, \tag{3.1}$$

where  $p \geq 0$  and  $q > 0$  are constants.<sup>3</sup> To first order in the perturbation  $\epsilon$  introduced in the previous section,  $\tilde{R}(\theta, \varphi) = R(\theta, \varphi) + \delta R(\theta, \varphi)$ ,  $\tilde{Z}(\theta, \varphi) = Z(\theta, \varphi) + \delta Z(\theta, \varphi)$ , and the Fourier coefficients of  $\delta R$  and  $\delta Z$  are given by

$$\left. \begin{aligned} \delta R_{m,n} &= \frac{1}{2\pi^2} \int \int \epsilon R_\theta \cos(m\theta - n\varphi) \, d\theta \, d\varphi, \\ \delta Z_{m,n} &= \frac{1}{2\pi^2} \int \int \epsilon Z_\theta \sin(m\theta - n\varphi) \, d\theta \, d\varphi, \end{aligned} \right\} \tag{3.2}$$

where subscripts indicate partial derivatives,  $R_\theta = \partial R / \partial \theta$ . The first-order variation in the spectral width thus becomes

$$\delta M = g^{-1} \int I(\theta, \varphi) \epsilon \, d\theta \, d\varphi, \tag{3.3}$$

<sup>3</sup>In the SPEC code (Hudson *et al.* 2012), it is defined without the normalization, i.e.  $M \equiv \sum_{m,n} m^{(p+q)} (R_{m,n}^2 + Z_{m,n}^2)$ .

where

$$\left. \begin{aligned} g &= \pi^2 \sum_{m,n} m^p (R_{mn}^2 + Z_{mn}^2), \\ I(\theta, \varphi) &= X(\theta, \varphi)R_\theta + Y(\theta, \varphi)Z_\theta, \\ X(\theta, \varphi) &= \sum_{m,n} m^p (m^q - M)R_{m,n} \cos(m\theta - n\varphi), \\ Y(\theta, \varphi) &= \sum_{m,n} m^p (m^q - M)Z_{m,n} \sin(m\theta - n\varphi). \end{aligned} \right\} \tag{3.4}$$

Note that the  $m = 0$  terms do not contribute to the Fourier sums and that the spectral width assumes its minimum when  $I(\theta, \varphi) = 0$ . This constraint is imposed to the requisite accuracy by Fourier expanding  $I(\theta, \varphi)$  and requiring a number  $m^*$  of the Fourier coefficients  $I_{mn}$  to vanish, thus effectively removing  $m^*$  degrees of freedom from the representation (Hirshman & Meier 1985).

**4. An explicit boundary representation**

The method of spectral condensation is optimal in the sense that it minimizes the spectral width of the representation, but it adds conceptual and computational complexity. The number of coefficients in the representation (1.1) remains high, although the constraints  $I_{mn} = 0$  effectively restrict the search to a submanifold of lower dimensionality, and the system of equations corresponding to these constraints must, in general, be solved numerically. In this and the next section (§ 5), we explore a simpler and more explicit construction as a possible alternative.

There are, of course, infinitely many ways of making the choice of poloidal angle unique, some of which have been proposed before, see e.g. Hirshman & Weitzner (1985), Hirshman & Breslau (1998) and Carlton-Jones, Paul & Dorland (2021). A particularly simple choice could be to express the vertical coordinate as

$$Z(\theta, \varphi) = a(\varphi) + b(\varphi) \sin \theta. \tag{4.1}$$

If the functions  $a$  and  $b$  are Fourier decomposed,

$$\left. \begin{aligned} a(\varphi) &= \sum_{n=1}^N a_n \sin n\varphi, \\ b(\varphi) &= \sum_{n=0}^N b_n \cos n\varphi, \end{aligned} \right\} \tag{4.2}$$

one finds that this representation is of the same form as (1.1) but with only two poloidal harmonics,

$$Z(\theta, \varphi) = \sum_{m=0}^1 \sum_{n=-N}^N Z_{m,n} \sin(m\theta - n\varphi), \tag{4.3}$$

which are equal to

$$nZ_{0n} = -a_n, \quad Z_{1n} = \frac{b_{|n|}}{2}. \tag{4.4a,b}$$

In each poloidal cross-section of the plasma surface, the poloidal angle  $\theta$  thus defined is the polar angle of the horizontal projection on a circle with a diameter equal to the

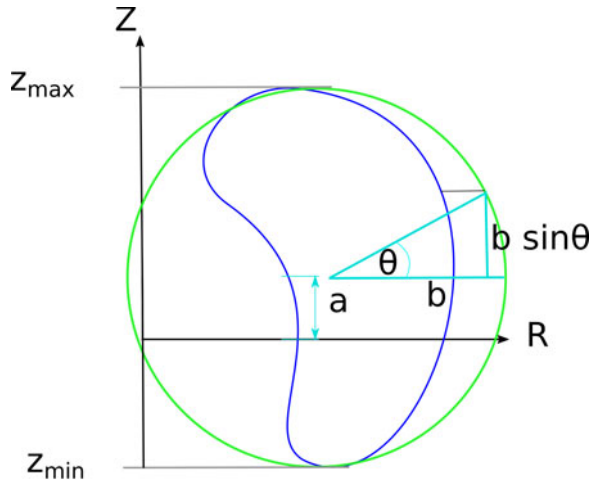


FIGURE 1. Circle (green) with radius  $b = (z_{\max} - z_{\min})/2$ , twice the total extent in the Z-direction of the plasma boundary (blue). The poloidal angle is chosen to be equal to the polar angle of the horizontal projection of each boundary point on this circle.

vertical extent of the surface, see figure 1. This choice of representation, which removes the superfluous degrees of freedom, can produce all surface shapes without multiple minima and maxima in the vertical coordinate  $Z$  in each poloidal cross-section. The vast majority of all stellarators considered to date possess this property.

However, (4.3) suffers from another and more serious shortcoming: it cannot economically represent a classical stellarator. Such devices have an elliptical poloidal cross-section that rotates co- or counter-clockwise with increasing toroidal angle  $\varphi$ . This can be seen by introducing a rotating coordinate system,

$$\left. \begin{aligned} \rho &= (R - R_0) \cos \alpha \varphi + Z \sin \alpha \varphi, \\ \zeta &= -(R - R_0) \sin \alpha \varphi + Z \cos \alpha \varphi, \end{aligned} \right\} \quad (4.5)$$

where  $\alpha$  is a constant determining the rate of rotation. For a classical stellarator, it is equal to half the number of toroidal periods  $N_p$  of the device,  $\alpha = N_p/2$ , so that the cross-section rotates by 180 degrees in one period. In these coordinates, a surface with rotating elliptical boundary is represented by

$$\left. \begin{aligned} \rho(\theta, \varphi) &= A \cos \theta, \\ \zeta(\theta, \varphi) &= B \sin \theta, \end{aligned} \right\} \quad (4.6)$$

where  $A$  and  $B$  denote the semi-axes. In our original coordinates, we obtain

$$\left. \begin{aligned} R(\theta, \varphi) &= R_0 + \frac{A - B}{2} \cos(\theta - \alpha \varphi) + \frac{A + B}{2} \cos(\theta + \alpha \varphi), \\ Z(\theta, \varphi) &= \frac{B - A}{2} \sin(\theta - \alpha \varphi) + \frac{A + B}{2} \sin(\theta + \alpha \varphi). \end{aligned} \right\} \quad (4.7)$$

Hence, it is clear that  $Z_{1,-1} \neq Z_{1,1}$  in contradiction to (4.4a,b), which can only mean that the poloidal coordinate  $\theta$  used in (4.3) cannot coincide with the corresponding one in (4.7). Although the former representation can describe any stellarator-symmetric surface,

it needs *many* harmonics  $R_{m,n}$  for a surface with rotating elliptical cross-section. Close to the magnetic axis, most stellarators have this property, making this shortcoming serious indeed.

Fortunately, it is easily overcome by applying a representation similar to (4.1) in the rotating coordinate system. This leads to the prescription

$$\left. \begin{aligned} R(\theta, \varphi) &= R_0(\varphi) + \rho(\theta, \varphi) \cos \alpha\varphi - \zeta(\theta, \varphi) \sin \alpha\varphi, \\ Z(\theta, \varphi) &= Z_0(\varphi) + \rho(\theta, \varphi) \sin \alpha\varphi + \zeta(\theta, \varphi) \cos \alpha\varphi, \end{aligned} \right\} \quad (4.8)$$

with

$$\left. \begin{aligned} \rho(\theta, \varphi) &= \sum_{m,n} \rho_{m,n} \cos(m\theta + n\varphi - \alpha\varphi), \\ \zeta(\theta, \varphi) &= b(\varphi) \sin(\theta - \alpha\varphi) = \sum_{n=0}^N b_n \cos n\varphi \sin(\theta - \alpha\varphi), \end{aligned} \right\} \quad (4.9)$$

which is our final recipe for unambiguously and economically representing a stellarator-symmetric toroidal surface, see figure 2. In terms of our original representation (1.1), the coefficients become for  $m \neq 0$

$$R_{m,n} = \frac{1}{2} (\rho_{m,-n+2\alpha} + \rho_{m,-n}) + \frac{\delta_{m1}}{4} (b_n + b_{-n} - b_{n-2\alpha} - b_{-n+2\alpha}), \quad (4.10)$$

$$Z_{m,n} = \frac{1}{2} (\rho_{m,-n} - \rho_{m,-n+2\alpha}) + \frac{\delta_{m1}}{4} (b_n + b_{-n} + b_{n-2\alpha} + b_{-n+2\alpha}). \quad (4.11)$$

Specifically, if  $\alpha = 1/2$ , we have

$$R_{m,n} = \frac{1}{2} (\rho_{m,-n+1} + \rho_{m,-n}) + \frac{\delta_{m1}}{4} (b_n + b_{-n} - b_{n-1} - b_{-n+1}), \quad (4.12)$$

$$Z_{m,n} = \frac{1}{2} (\rho_{m,-n} - \rho_{m,-n+1}) + \frac{\delta_{m1}}{4} (b_n + b_{-n} + b_{n-1} + b_{-n+1}). \quad (4.13)$$

In our experience, and as we shall see in § 5, this simple prescription works very well in practice.

### 5. Numerical examples

In this section, we explore a few examples of increasing complexity and realism, comparing our recipe with the conventional approach.

#### 5.1. Simple axisymmetric (two-dimensional (2-D)) case

Our first aim is to gain insight into the optimization space using the original arbitrary-angle representation (1.1). Because only the poloidal angle  $\theta$  is arbitrary, this issue can be explored in a simpler, two-dimensional setting. We choose to target an axisymmetric torus with a unit circle as the poloidal cross-section. A simple penalty function  $Q$  that

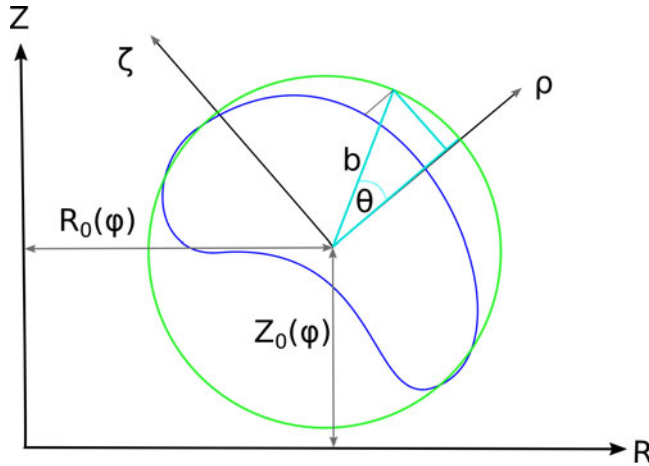


FIGURE 2. Circle (green) with radius  $b = (\zeta_{\max} - \zeta_{\min})/2$  and the boundary (blue). The poloidal angle  $\theta$  is the polar angle of the projection in the  $\rho$ -direction onto the circle.

is minimized by this surface is

$$Q[R, Z] := A^{-1} \oint ((R(\theta) - R_0)^2 + Z^2(\theta) - 1)^2 ds, \tag{5.1}$$

where

$$ds = R \sqrt{(R_\theta^2 + Z_\theta^2)} d\theta d\varphi. \tag{5.2}$$

Here the surface area is  $A := \oint ds$ , and the major radius is arbitrarily chosen to be  $R_0 = 1.5$ . We restrict  $R$  and  $Z$  to be axisymmetric:  $R_{mn} = Z_{mn} = 0$  for all  $n \neq 0$  and write

$$R = 1.5 + \sum_{m=1} R_m \cos(m\theta), \tag{5.3}$$

and

$$Z = \sum_{m=1} Z_m \sin(m\theta). \tag{5.4}$$

If  $Q$  is not normalized to the area  $A$ , an artificial minimum exists when the area becomes small. With the normalization, the penalty function  $Q$  approaches unity in the limit of vanishing  $R - R_0$  and  $Z$  (and thus vanishing surface area). The penalty function attains its sole minimum ( $Q = 0$ ) if  $(R - R_0)^2 + Z^2 = 1$ . This equation is satisfied by many different choices of  $R_m$  and  $Z_m$ .<sup>4</sup>

If all but the  $m = 1$  Fourier coefficients vanish, i.e. if  $Q = Q(R_1, Z_1, R_i = 0, Z_i = 0)$  for  $i > 0$ , the penalty function attains the global minimum for  $R_1 = Z_1 = 1$ , see figure 3, and this is, in general, the case when only one pair of coefficients  $(R_m, Z_m)$  is allowed to be non-zero, see figure 4.

More interesting and complex behaviour is observed if Fourier harmonics with several values of  $m$  are admitted, but one then faces the problem of graphically displaying the function  $Q$  of more than two variables. For instance, it is not easy to visualize how the cost

<sup>4</sup>Although this is the only global minimum,  $Q$  becomes arbitrarily small for bounded surfaces having very large area, e.g. for highly ‘wrinkled’ surfaces.

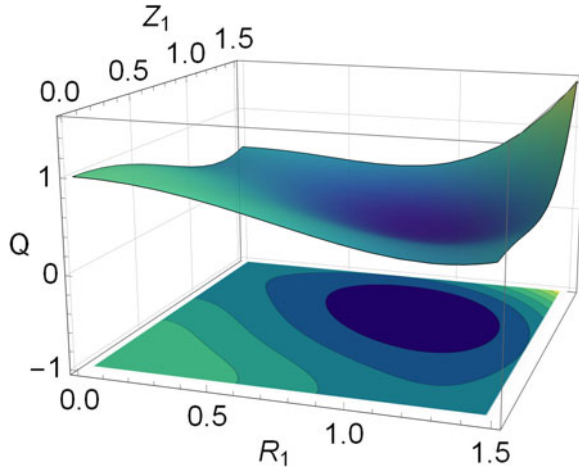


FIGURE 3. The cost function  $Q(R_1, Z_1)$  with respect to  $R_1$  and  $Z_1$  with all other Fourier harmonics equal to zero  $R_i = Z_i = 0, i > 1$ .

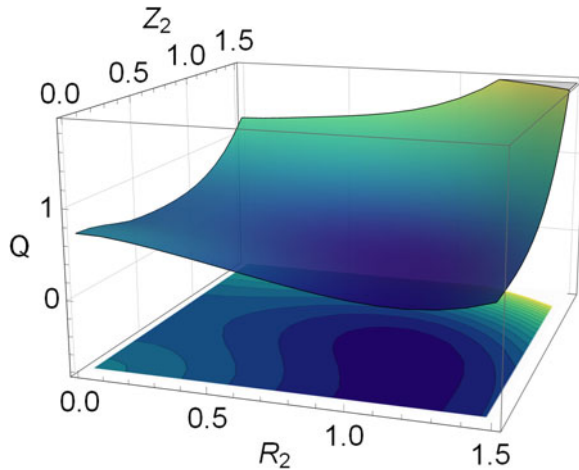


FIGURE 4. The cost function  $Q(R_1 = 0.0, R_2, Z_1 = 0.7, Z_2)$  with respect to  $R_2$  and  $Z_2$ .

function  $Q(R_1, R_2, Z_1, Z_2)$  depends on all four arguments. However, some insight can be gained by plotting the minimum of  $Q$  with respect to two of the arguments as a function of the two other ones, e.g. by considering the function

$$\tilde{Q}(R_1, Z_1) = \min_{R_2, Z_2} Q(R_1, R_2, Z_1, Z_2). \tag{5.5}$$

Considering four Fourier harmonics in this way reveals the existence of three local minima, see figure 5. Two of these correspond to the global minimum,  $R_1 = Z_1 = 1, R_2 = Z_2 = 0$  and  $R_1 = Z_1 = 0, R_2 = Z_2 = 1$ , and both correspond to the target surface, an axisymmetric torus with a unit circle cross-section, parametrized in two different ways. The third minimum is located at  $R_1 = 0.0, R_2 \approx 1.05, Z_1 = 1.15$  and  $Z_2 = 0.0$  with  $Q \approx 0.133$ . It corresponds to a surface with zero volume but finite area, see figure 6.

Increasing the number of poloidal harmonics  $m$  to three makes it more difficult to locate the local minima of the cost function. Without a global optimizer, one

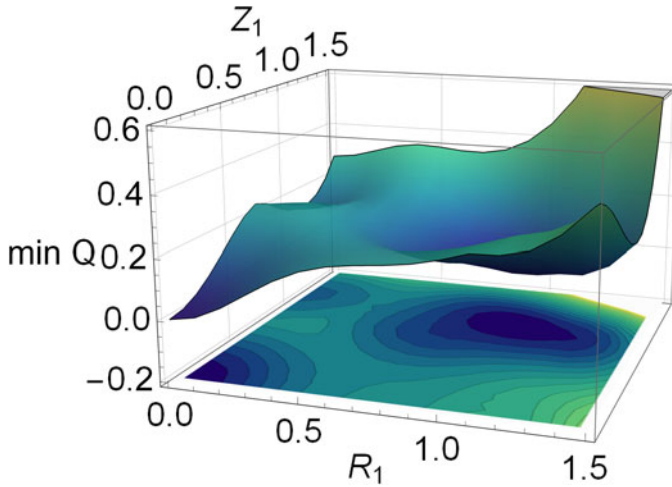


FIGURE 5. The minimized cost function  $\min_{R_2, Z_2} Q(R_1, R_2, Z_1, Z_2)$  with respect to  $R_1$  and  $Z_1$ .

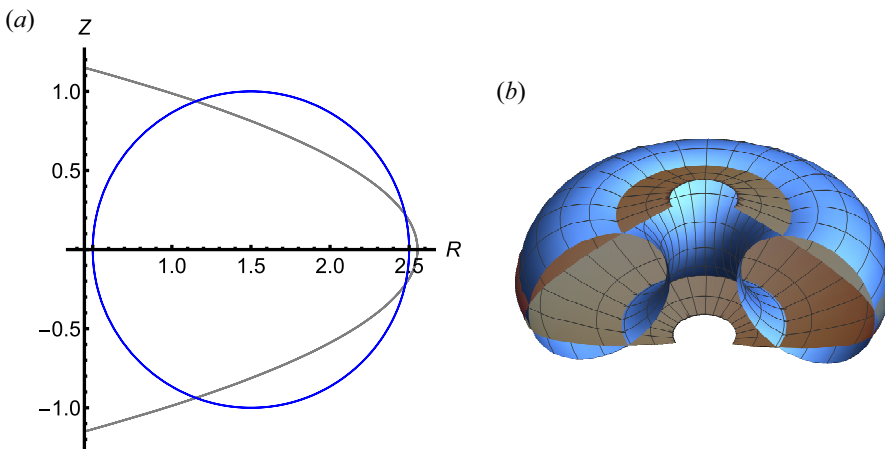


FIGURE 6. The three minima of  $Q(R_1, R_2, Z_1, Z_2)$ . Global minima (blue): axisymmetric torus with unit circle cross-section described by  $R_1 = Z_1 = 1, R_2 = Z_2 = 0$  and  $R_1 = Z_1 = 0, R_2 = Z_2 = 1$  ( $R_i = 0$  for all  $i > 2$ ). Local minimum (grey):  $R_1 = 0.0, R_2 \approx 1.05, Z_1 = 1.15$  and  $Z_2 = 0.0$ : (a) the poloidal cross-section; (b) three-dimensional (3-D) view.

encounters many local minima depending on the initial values chosen for the remaining Fourier coefficients. Using differential evolution, a global optimization routine, to obtain  $\min_{R_2, Z_2, R_3, Z_3} Q(R_1, R_2, R_3, Z_1, Z_2, Z_3)$ , one finds a landscape broadly similar to that found for the four-Fourier-coefficient case, see figure 7. In the neighbourhood of a local minimum, the global optimizer roughly finds similar values for  $(R_2, Z_2, R_3, Z_3)$ . In between the minima, depicted in figure 7, there is a transition region, where the global optimizer has to decide between two (or even more) competing local minima which can be challenging. When it jumps to a different local minimum, the landscape is typically not smooth. This type of scan has to be considered with caution. Most global optimization routines do not, in practice, guarantee a global minimum but sometimes end up in local ones. In local

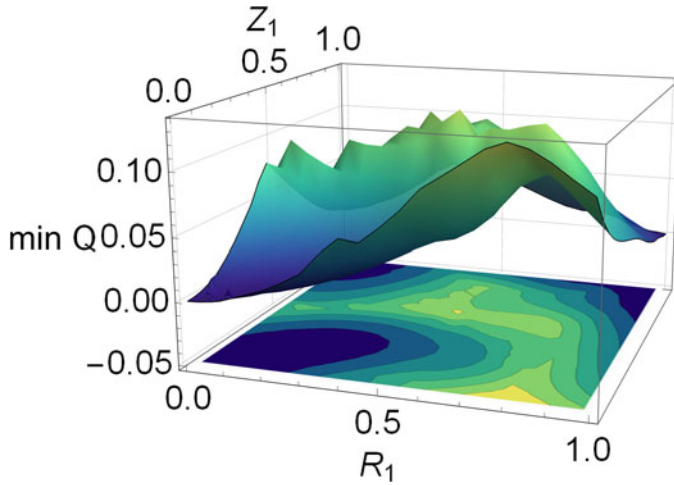


FIGURE 7. The minimized cost function  $\min_{R_2, Z_2, R_3, Z_3} Q(R_1, R_2, R_3, Z_1, Z_2, Z_3)$  with respect to  $R_1$  and  $Z_1$ . Differential Evolution, a global optimization routine, is used to find the minima.

optimization routines, this problem is of course still more acute, because the outcome generally depends on the initialization.

To visualize the difficulty of finding global minima, it is useful to fix two coefficients in the following  $R_1 (=0.18)$  and  $Z_1 (=0.4)$ , and study how the landscape depends on the remaining ones. We note that the function  $\min_{R_2, R_3, Z_2, Z_3} Q(R_1 = 0.18, R_2, R_3, Z_1 = 0.4, Z_2, Z_3)$  possesses five local minima with  $R_2$  and  $Z_2$  in the range 0.0–1.0, see figure 8, and line discontinuity, as can be seen in figure 8. To understand the discontinuity of  $\min_{R_2, R_3, Z_2, Z_3} Q(R_1 = 0.18, R_2, R_3, Z_1 = 0.4, Z_2, Z_3)$ , we plot the function  $Q(R_1 = 0.18, R_2 = x, R_3, Z_1 = 0.4, Z_2 = y, Z_3)$  with respect to  $R_3$  and  $Z_3$  for selected values for  $x$  and  $y$ , figure 9. The number of local minima varies with  $x$  and  $y$ . For  $(x, y) = (0.24, 0.39)$ , there are four local minima in the figure; for  $(x, y) = (0.5, 0.5)$ , there are two of them; and for  $(x, y) = (1, 1)$ , there is only one minimum. It is thus clear that a local optimizer that seeks local minima of the function  $Q(R_1 = 0.18, R_2, R_3, Z_1 = 0.4, Z_2, Z_3)$  will find different ones depending on the starting point for  $R_2, R_3, Z_2$  and  $Z_3$ . Abrupt changes (discontinuity) in  $\min_{R_2, R_3, Z_2, Z_3} Q(R_1 = 0.18, R_2, R_3, Z_1 = 0.4, Z_2, Z_3)$  appear when a local minimum disappears and the optimizer finds a different one.

The representation proposed in § 4 leads to much more benign results when applied to the model problem (5.1). Restricting the optimization space to axisymmetric designs leads to

$$\left. \begin{aligned} R &= 1.5 + \sum_{m=1} R_m \cos(m\theta), \\ Z &= Z_1 \sin(\theta). \end{aligned} \right\} \tag{5.6}$$

This time, we find that the landscape of the minimum penalty function  $\min Q$  does not change much when the number of Fourier harmonics of  $R$  is increased. In the case of four Fourier harmonics,  $Q(R_1, R_2, R_3, Z_1)$ , there is one global minimum at  $R_1 = 1, R_2 = 0, R_3 = 0, Z_1 = 1$  and a second shallow local minimum near  $R_1 = 0$  and  $Z_1 = 1.0$ , see figure 10. This local minimum disappears when more Fourier harmonics are added. Importantly, the outcome is similar whether a local and global optimization algorithm

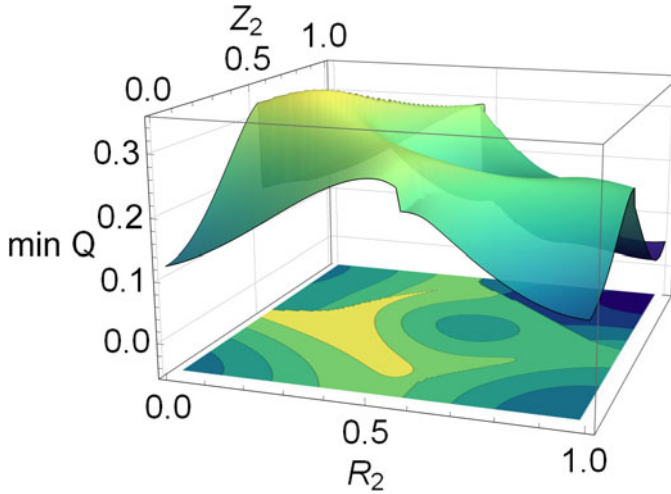


FIGURE 8. The locally minimized cost function  $\min_{R_3, Z_3} Q(R_1 = 0.18, R_2, R_3, Z_1 = 0.4, Z_2, Z_3)$  as a function of  $R_2$  and  $Z_2$ .

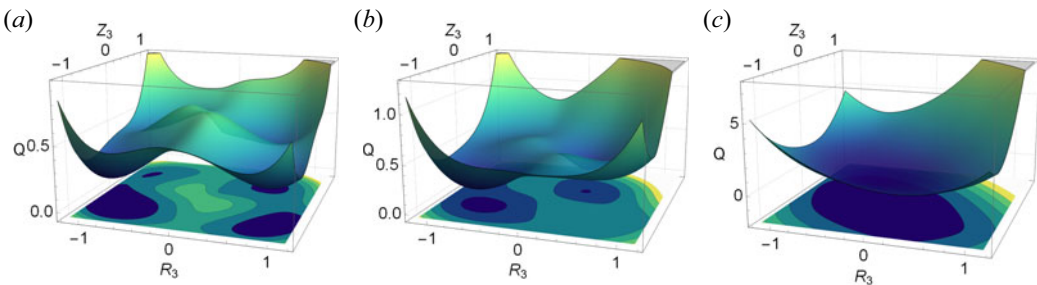


FIGURE 9. The cost function  $Q(R_1 = 0.18, R_2 = x, R_3, Z_1 = 0.4, Z_2 = y, Z_3)$  with respect to  $R_3$  and  $Z_3$ : (a)  $x = 0.24$  and  $y = 0.39$ ; (b)  $x = 0.5$  and  $y = 0.5$ ; (c)  $x = 1.0$  and  $y = 1.0$ .

is employed, see figures 11(a) and 11(b), respectively, making it much easier to find the minima numerically.

### 5.2. Fourier representation of stellarators

We now turn to examples of explicit choices of the coefficients  $R_{m,n}, Z_{m,n}, \rho_{m,n}$  and  $b_n$ , corresponding to stellarator plasma boundaries that have been explored in this context in the past. We begin with examples from Hirshman & Meier (1985), who analysed shapes using spectral condensation, thus providing a convenient point of comparison with this technique.

We start with a planar D-shaped boundary given by  $R = -0.23 + 0.989 \cos \theta + 0.137 \cos 2\theta$  and  $Z = 1.41 \sin \theta - 0.109 \sin 2\theta$  after spectral condensation (Hirshman & Meier 1985). We use Fourier decomposition to obtain the coefficients in our unique boundary representation that reproduce this boundary, restricting the number of modes  $m$  to be such that all the coefficients exceed 0.01. The result is  $R_{00} = -0.306, b_0 = 1.426$  and  $\rho = 0.957 \cos \theta + 0.207 \cos 2\theta + 0.032 \cos 3\theta$ .

Hirshman and Meier also considered a bean-shaped surface given by  $R = -0.320 + 1.115 \cos \theta + 0.383 \cos 2\theta - 0.0912 \cos 3\theta + 0.0358 \cos 4\theta - 0.0164 \cos 5\theta$  and  $Z =$

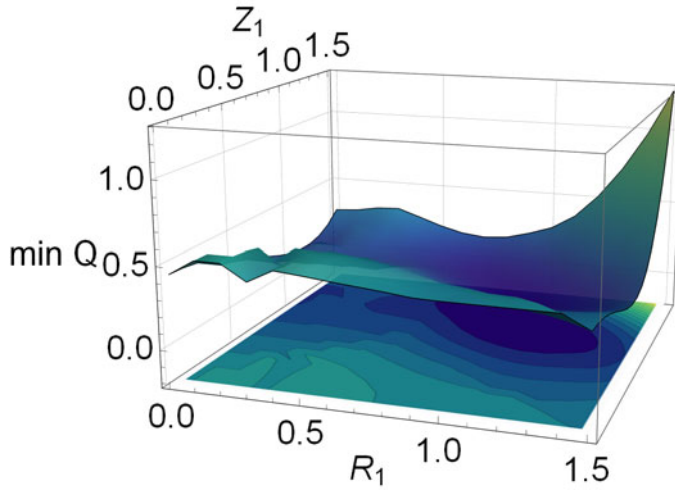


FIGURE 10. The minimized cost function  $\min_{R_2, R_3} Q(R_1, R_2, R_3, Z_1)$  with respect to  $R_1$  and  $Z_1$ .

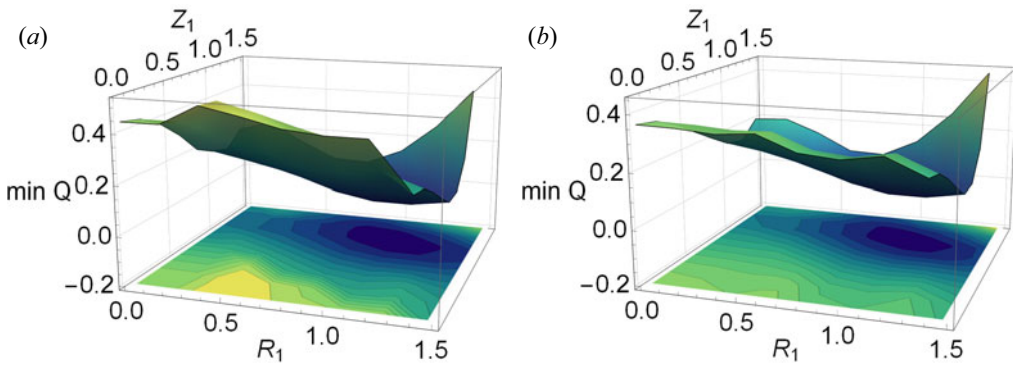


FIGURE 11. The minimized cost function  $\min_{R_2, R_3, R_4, R_5} Q(R_1, R_2, R_3, R_4, R_5, Z_1)$  with respect to  $R_1$  and  $Z_1$ : (a) using a non-global optimization algorithm; (b) using Differential Evolution – a global optimization routine.

$1.408 \sin \theta + 0.154 \sin 2\theta - 0.0264 \sin 3\theta$  after spectral condensation. Applying our representation to this case, we obtain  $R_{00} = -0.184$ ,  $b_0 = 1.419$  and  $\rho = 1.184 \cos \theta + 0.208 \cos 2\theta - 0.143 \cos 3\theta + 0.064 \cos 4\theta - 0.032 \cos 5\theta + 0.011 \cos 6\theta$ . Our representation thus needs even fewer Fourier harmonics than this spectral condensation.<sup>5</sup>

Finally, we consider a representative example from Wendelstein 7-X, where the magnetic field in the so-called standard configuration was calculated using an equilibrium solver in free-boundary mode. As shown in figure 13, the resulting plasma boundary can be faithfully reproduced with mode numbers  $m \leq 5$  and  $|n| \leq 3$ .

Thus, the representation proposed in § 4 can accurately and economically reproduce relevant plasma boundary shapes, including Wendelstein 7-X and other cases studied earlier in the literature. It does not always need as few Fourier harmonics as spectral

<sup>5</sup>Hirsman and Meier also consider a third case, a so-called belt pinch boundary, which cannot be reproduced by our boundary representation as it has multiple minima and maxima in the vertical coordinate.

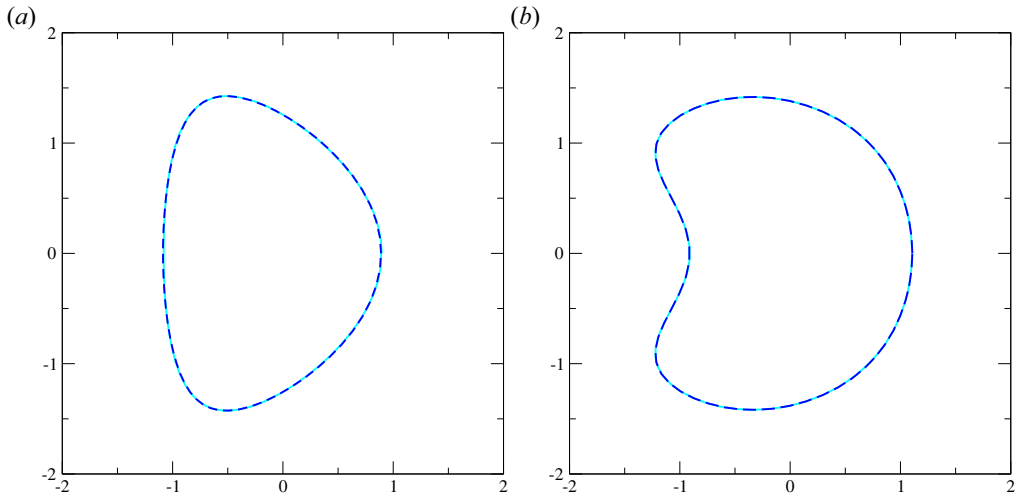


FIGURE 12. D shape and bean shape reproduced based on Hirshman & Meier (1985), where the solution of our boundary representation overlaps with the original boundary: (a) D shape; (b) Bean shape.

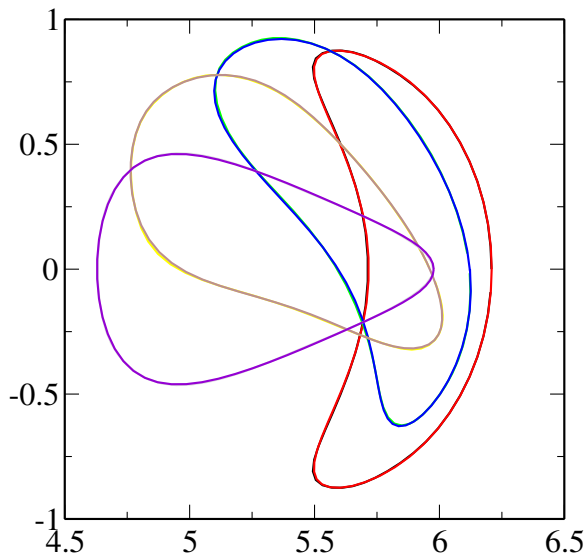


FIGURE 13. The boundary at different toroidal angle of Wendelstein 7-X. The original overlaps mostly with the replication.

condensation, but for ‘reasonable’ shapes, it appears comparable in efficiency and avoids the need for computational optimization, which is an integral part of the spectral condensation technique.

### 5.3. Application to 3-D stellarator optimization

Finally, we put our boundary representation to the test in a real stellarator optimization problem, where the plasma boundary serves as the input for a fixed-boundary equilibrium calculation and is adjusted iteratively until a target function reflecting plasma performance

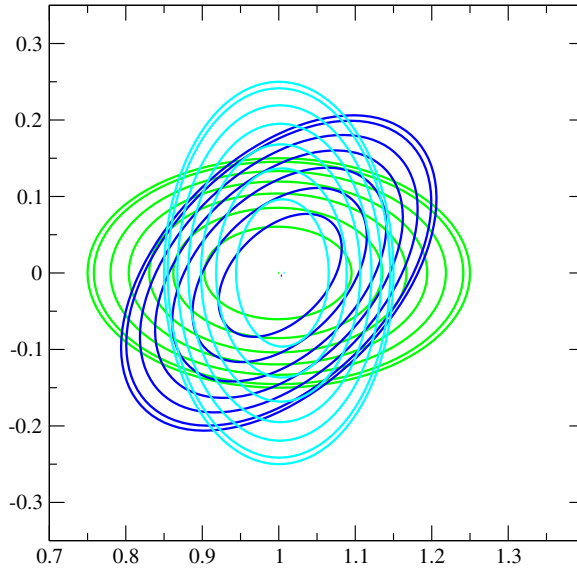


FIGURE 14. Flux surfaces at different toroidal cross-sections of rotating ellipse at toroidal angle  $\varphi = 0^\circ$  (green),  $45^\circ$  (dark blue) and  $90^\circ$  (cyan).

has been minimized. As described in the introduction, § 1, such optimization calculations have, in the past, usually been performed with the ambiguous boundary representation (1.1).

We start the optimization with a rotating elliptical boundary, figure 14, and use the optimization code ROSE (Drevlak *et al.* 2019) with the equilibrium code VMEC and a non-gradient, non-global optimization algorithm (Brent). The target rotational transform is chosen to be 0.25 on axis and 0.35 at the plasma boundary, and in addition, we require the magnetic well to exceed a certain threshold (0.1) and the toroidal projection of the plasma boundary to be convex in every point.

As is usual in this type of optimization, the target function  $f$  is a weighted sum of squares,

$$f = \sum_i w_i (F_i - \tilde{F}_i)^2, \quad (5.7)$$

where  $F_i$  is the value for criterion  $i$ ,  $\tilde{F}_i$  the corresponding target value and  $w_i$  the  $i$ 'th weight, which can be adjusted to obtain various different optimal (Pareto) points.

Of course, the performance of the optimization depends on the exact choice of  $w_i$  and  $F_i$  as well as the initial condition, but we find that the results turn out much better, and more quickly, with the novel representation than with the standard one used in VMEC. With the same weights chosen for both cases, we typically obtain a penalty value  $f$  that is two orders of magnitude smaller when the new boundary representation is employed. The resulting configuration is thus significantly different, and much better, than that obtained with the conventional method. An example of how the plasma boundaries differ is shown in figure 15. In this example, all the aims of the optimization were attained when the novel scheme was used, whereas the usual one did not succeed in achieving the prescribed rotational transform and a non-concave plasma boundary. Similar results have also been found with other, more complicated, optimization targets.

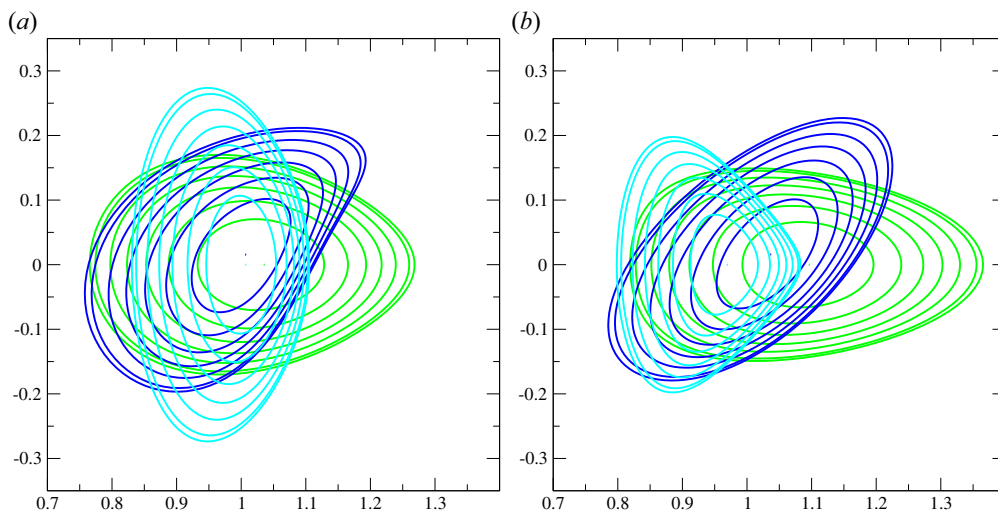


FIGURE 15. The poloidal cross-sections of optimized plasma boundary and flux surfaces with simple penalty function for the toroidal angles  $\varphi = 0^\circ$  (green),  $45^\circ$  (dark blue) and  $90^\circ$  (cyan): (a) cross-sections of optimized plasma boundary using standard VMEC boundary representation; (b) cross-sections of optimized plasma boundary using unique boundary representation described in § 4.

## 6. Conclusions

In summary, the usual Fourier series representation of the plasma boundary used in stellarator optimization contains much redundancy owing to the arbitrariness of the poloidal angle. This redundancy grows exponentially with the number of terms in the series and unnecessarily increases the dimensionality of the search. It causes a plethora of local minima to appear in the optimization landscape, as can be illustrated with simple 2-D examples. The situation can be remedied by making the poloidal angle unique, but some care must be taken to ensure that simple stellarator shapes can still be represented in an economical way. When this is done, local minima are eliminated and the optimization proceeds more rapidly than with the usual representation. The outcome also tends to be better, especially if a non-global optimization algorithm is used.

Our specific boundary parametrization (4.10)–(4.11) is simple and intuitive, and requires less computation than the spectral condensation method, but it cannot describe stellarator boundaries with multiple maxima in the  $\zeta$ -direction. Such boundaries are however highly unusual, and the representation can easily be generalized to include such shapes.

## Acknowledgements

The primary author would like to thank B. Kugelmann, G. Plunk and B. Shanahan for helpful conversations.

*Editor William Dorland thanks the referees for their advice in evaluating this article.*

## Funding

This work has been carried out in the framework of the EUROfusion Consortium and has received funding from the Euratom research and training programmes 2014–2018 and 2019–2020 under grant agreement no. 633053. It was also supported by a grant from

the Simons Foundation (560651, P.H.). The views and opinions expressed herein do not necessarily reflect those of the European Commission.

### Declaration of interests

The authors report no conflict of interest.

### REFERENCES

- CARLTON-JONES, A., PAUL, E.J. & DORLAND, W. 2021 Computing the shape gradient of stellarator coil complexity with respect to the plasma boundary. *J. Plasma Phys.* **87** (2), 905870222.
- DREVLAK, M., BEIDLER, C.B., GEIGER, J., HELANDER, P. & TURKIN, Y. 2019 Optimisation of stellarator equilibria with ROSE. *Nucl. Fusion* **59** (1), 016010.
- HELANDER, P. 2014 Theory of plasma confinement in non-axisymmetric magnetic fields. *Rep. Prog. Phys.* **77** (8), 087001.
- HIRSHMAN, S.P. & BRESLAU, J. 1998 Explicit spectrally optimized Fourier series for nested magnetic surfaces. *Phys. Plasmas* **5** (7), 2664–2675.
- HIRSHMAN, S.P. & MEIER, H.K. 1985 Optimized fourier representations for three-dimensional magnetic surfaces. *Phys. Fluids* **28** (5), 1387–1391, <https://aip.scitation.org/doi/pdf/10.1063/1.864972>.
- HIRSHMAN, S.P. & WEITZNER, H. 1985 A convergent spectral representation for three-dimensional inverse magnetohydrodynamic equilibria. *Phys. Fluids* **28** (4), 1207–1209, <https://aip.scitation.org/doi/pdf/10.1063/1.864998>.
- HIRSHMAN, S. & VAN RIJ, W. 1986 3-dimensional free-boundary calculations using a spectral Greens-function method. *Comput. Phys. Commun.* **43** (1), 143–155.
- HIRSHMAN, S. & WHITSON, J. 1983 Steepest-descent moment method for 3-dimensional magnetohydrodynamic equilibria. *Phys. Fluids* **26** (12), 3553–3568.
- HUDSON, S., DEWAR, R., DENNIS, G., HOLE, M., MCGANN, M., VON NESSI, G. & LAZERSON, S. 2012 Computation of multi-region relaxed magnetohydrodynamic equilibria. *Phys. Plasmas* **19** (11), 112502.
- KRUSKAL, M. & KULSRUD, R. 1958 Equilibrium of a magnetically confined plasma in a toroid. *Phys. Fluids* **1** (4), 265–274.
- LEE, D., HARRIS, J., HIRSHMAN, S. & NEILSON, G. 1988 Optimum fourier representations for stellarator magnetic flux surfaces. *Nucl. Fusion* **28** (8), 1351–1364.
- NÜHRENBURG, J. & ZILLE, R. 1988 Quasi-helically symmetric toroidal stellarators. *Phys. Lett. A* **129** (2), 113–117.